














Rapid growth of Aitken-mode particles during Arctic summer by fog chemical processing and its implication

Simonas Kecorius ^{a,b,*}, Erik H. Hoffmann ^c, Andreas Tilgner ^c, Carola Barrientos-Velasco ^d, Manuela van Pinxteren ^c, Sebastian Zeppenfeld ^c, Teresa Vogl ^e, Leizel Madueño ^a, Mario Lovrić ^f, Alfred Wiedensohler ^a, Markku Kulmala ^g, Pauli Paasonen ^g and Hartmut Herrmann ^{c,*}

^aAtmospheric Microphysics, Leibniz Institute for Tropospheric Research (TROPOS), Leipzig 04318, Germany

^bPresent address: Institute of Epidemiology, Helmholtz Zentrum München—German Research Center for Environmental Health, Neuherberg 85764, Germany

^cAtmospheric Chemistry Department, Leibniz Institute for Tropospheric Research (TROPOS), Leipzig 04318, Germany

^dDepartment of Remote Sensing of Atmospheric Processes, Leibniz Institute for Tropospheric Research (TROPOS), Leipzig 04318, Germany

^eInstitute of Meteorology, Universität Leipzig, Leipzig 04103, Germany

^fDepartment of Methods and Algorithms for AI, Know-Center, Graz 8010, Austria

^gInstitute for Atmospheric and Earth System Research/Physics, Faculty of Science, University of Helsinki, Helsinki 00014, Finland

*To whom correspondence should be addressed: Email: simonas.kecorius@helmholtz-muenchen.de; herrmann@tropos.de

Edited By: Yannis Yortsos

Abstract

In the Arctic, new particle formation (NPF) and subsequent growth processes are the keys to produce Aitken-mode particles, which under certain conditions can act as cloud condensation nuclei (CCNs). The activation of Aitken-mode particles increases the CCN budget of Arctic low-level clouds and, accordingly, affects Arctic climate forcing. However, the growth mechanism of Aitken-mode particles from NPF into CCN range in the summertime Arctic boundary layer remains a subject of current research. In this combined Arctic cruise field and modeling study, we investigated Aitken-mode particle growth to sizes above 80 nm. A mechanism is suggested that explains how Aitken-mode particles can become CCN without requiring high water vapor supersaturation. Model simulations suggest the formation of semivolatile compounds, such as methanesulfonic acid (MSA) in fog droplets. When the fog droplets evaporate, these compounds repartition from CCNs into the gas phase and into the condensed phase of nonactivated Aitken-mode particles. For MSA, a mass increase factor of 18 is modeled. The postfog redistribution mechanism of semivolatile acidic and basic compounds could explain the observed growth of >20 nm h⁻¹ for 60-nm particles to sizes above 100 nm. Overall, this study implies that the increasing frequency of NPF and fog-related particle processing can affect Arctic cloud properties in the summertime boundary layer.

Keywords: new particle formation, Arctic fog, aqueous-phase processing, aerosol growth, cloud condensation nuclei

Significance Statement

In the Arctic, processes leading to more cloud condensation nuclei (CCNs) are crucial for radiative cloud properties and Arctic climate. The short lifetime and limited condensable vapors often prevent Aitken-mode particles from growing rapidly into CCN range. In the summer, Aitken-mode particles can activate to cloud droplets above the boundary layer, when accumulation-mode particle concentrations are low, enabling higher supersaturation. Near the ocean surface, supersaturations are generally lower, requiring the particles to be larger to activate. Observations showed a rapid growth of Aitken-mode particles after fog evaporation to sizes beyond 80 nm where they are more likely to act as CCN. This work reveals that the postfog growth of Aitken particles results from chemical in-fog production of semivolatile compounds and postfog repartitioning processes.

Introduction

High-latitude regions have experienced a well-documented and stronger-than-average increase in near-surface temperature (1–3). Resulting changes in the Arctic include, but are not limited to, (i) the development of melt ponds, (ii) an increase in the mean speed of sea-ice flow, and (iii) deformation and decline in multiyear sea-ice cover (4–6). Such changes are expected to have impacts on the Arctic ecosystem as a whole (7), local and global climate (8, 9),

worldwide economies (10), and shifting geopolitical interests (11). While some of these transformations may result in new opportunities (e.g. in maritime transport) (12), the warming Arctic and its effects can be seen as one of the greatest environmental challenges of the 21st century.

To determine the energy flows and surface energy budget in the Arctic, a comprehensive understanding of aerosol effects on clouds and their properties is required. In general, clouds in the

Competing Interest: The authors declare no competing interest.

Received: July 15, 2022. **Revised:** March 21, 2023. **Accepted:** April 3, 2023

© The Author(s) 2023. Published by Oxford University Press on behalf of National Academy of Sciences. This is an Open Access article distributed under the terms of the Creative Commons Attribution-NonCommercial-NoDerivs licence (<https://creativecommons.org/licenses/by-nc-nd/4.0/>), which permits non-commercial reproduction and distribution of the work, in any medium, provided the original work is not altered or transformed in any way, and that the work is properly cited. For commercial re-use, please contact journals.permissions@oup.com

Arctic warm the surface for most of the year (13, 14). Although studies on Arctic clouds do exist (15–17), the role of aerosol particles and their effect on Arctic clouds remains uncertain. This is likely due to insufficient and only episodic measurements in the region (18). Because of the high sensitivity of Arctic clouds to the number concentration of aerosol particles upon which clouds form (19), identifying and understanding the potential sources of cloud condensation nuclei (CCNs) in the high Arctic is of high importance. Investigations on cloud formation and quantification of CCN sources are required to improve cloud-related Arctic surface radiative budget parameterizations and model predictions.

Because primary particle sources are scarce in the Arctic, atmospheric new particle formation (NPF) here is one of the main processes producing a high number of aerosols, at times up to three orders of magnitude higher than the background concentration (20). However, in the Arctic, formation and growth rates (GR) of aerosol particles are considerably smaller compared with anthropogenically influenced environments (21). Low concentrations of condensable vapors hinder newly produced particle growth to sizes >80 nm, a size at which Aitken-mode particles can act as CCN without requiring high water vapor supersaturation (S) to exceed the critical diameter for activation. This, in turn, may decrease their atmospheric relevance. Under ambient noncloud conditions, observed GR of Aitken-mode particles in the pristine Arctic environment are usually 0.2 to 1.2 nm h⁻¹ (20, 22). Occasional GR > 2 nm h⁻¹ were also observed (23) and were linked to condensable organic vapors. While some model studies have highlighted the importance of dimethyl sulfide (DMS) oxidation in enhancing aerosol particle growth between 60 and 200 nm (24–26), others argue against it (27). This may be because the applied DMS oxidation schemes do not consider the importance of aqueous-phase chemistry processes on the cloud droplet number concentration (28, 29). It remains unclear how biogenic emissions and resulting semivolatile compounds (SVCs) affect the growth of newly formed particles into CCN size ranges >80 nm in pristine Arctic environments and to what extent DMS oxidation is involved (30).

It is important to note that particles below 50 nm can act as CCN [see Abbatt et al., Komppula et al., Croft et al., Leaitch et al., Pöhlker et al., Kerminen et al., and Koike et al. (30–36) and references therein] under Arctic conditions. It is known that Aitken-mode particles can particularly activate to cloud droplets during summertime conditions in the upper part of the Arctic boundary layer due to higher S and correspondingly lower droplet activation diameters (33, 36). The activation of smaller particles in clouds at higher altitudes is additionally driven by low accumulation-mode particle number concentration (PNC), which increases cloud S > 0.3%. Near the ocean surface, however, cloud or fog S is generally lower (33, 36), requiring certain conditions [e.g. low accumulation-mode PNC; updraft wind speed in a range of 0.3 m s⁻¹ (37); particle diameter in a range of 80 nm] for particles to activate. Although possible, such conditions may be less frequent (37, 38) than other mechanisms contributing to increased CCN concentrations (e.g. NPF followed by particle processing in fogs). Moreover, the success of newly formed particles in becoming CCNs depends on their survival in the atmosphere. The ultra-fine particles can be efficiently removed over the open water surface by coagulation with fog droplets (22). With that said, newly formed particles in general seem to be persistent and reappear after fog has dissipated (see also Fig. 1). In addition, Arctic fog may create favorable conditions (e.g. via in-cloud chemical processes) for efficient formation of secondary aerosol mass and SVCs. Recent measurements onboard the research vessel

(RV) Polarstern in the Arctic showed regional NPF (20) and rapid unexpected growth of Aitken-mode particles after extended Arctic fog periods. Such postfog growth processes can also be seen in a recent study (22), however, with no further investigation.

Due to a changing Arctic climate, NPF events and fog occurrence are predicted to increase, particularly in marginal sea ice zones (23, 39–41). Accordingly, the rapid increase in <60 nm particles observed in our study may become a dominant source of CCN; thus, it is important to understand their linked processes in more detail. The goals of this work are (i) to investigate unexpected observed growth of Aitken-mode particles, (ii) to provide evidence for the role of chemical in-fog and physical postfog processes, and (iii) to investigate the radiative responses of more CCN-active particles. To this end, all in situ observations are comprehensively studied, and the fog-related growth of Aitken-mode particles is simulated with an advanced multiphase chemistry model, while the radiative effects were simulated with a 1D radiative transfer model. The implications of the study findings are discussed with regard to particle growth processes and increased CCN number concentration. Finally, given the high frequency of occurrences of low-level clouds and fogs in the Arctic summer (41–43) and the increasing frequency of NPF episodes (23, 40, 41), the potential implications of the observed particle growth for further Arctic warming are discussed.

Results and discussion

Particle properties related to the fog events

Aitken-mode particle growth was observed following a regional NPF event (occurring at sea level; there was no particle entrainment from aloft) and subsequent fog formation in the summer Arctic, suggesting secondary aerosol mass formation through in-fog and postfog processes. This led to an investigation of the processes for Aitken-mode particles to grow in size, which can result in a CCN concentration increase in the summer Arctic. A detailed description of NPF events observed during the two-leg cruise in the Fram Strait and Barents Sea in the vicinity of Svalbard (Norway) from 2017 May to July, onboard the German RV Polarstern (PS106) was reported in a previous study (20). The [supplementary material](#) provides data on the physical and chemical properties of aerosol particles relevant only to the present study.

The rapid growth of Aitken-mode particles from ~60 to >100 nm (with GR > 20 nm h⁻¹) was observed when the following sequence of events occurred: (i) NPF and subsequent particle growth into the Aitken-mode; (ii) fog formation (lasting >10 min, required to produce SVCs); and (iii) fog evaporation. Although several regional NPF (involving aerosol particle formation and initial growth; Fig. S1) and multiple fog events were observed during the campaign, two episodes fulfilled all of the criteria for the rapid growth: an episode on 2017 June 1–2 (Fig. 1) and another episode on 2017 June 19–20 (Fig. S2). It should be noted that the fog events mentioned contained liquid droplets because the median temperature during the measurement campaign was 0.8°C (25th percentile—negative 2°C). The fact that two events of this kind occurred within 3 weeks during the measurement campaign suggests that the observed phenomenon is not a rare event. From a literature review on Arctic NPF and fog observations, it can be concluded that such combined conditions (NPF and subsequent fog occurrence) are rather frequent because of the commonly observed temporal relation between Arctic summer NPF and fog (see the [supplementary material](#) for details).

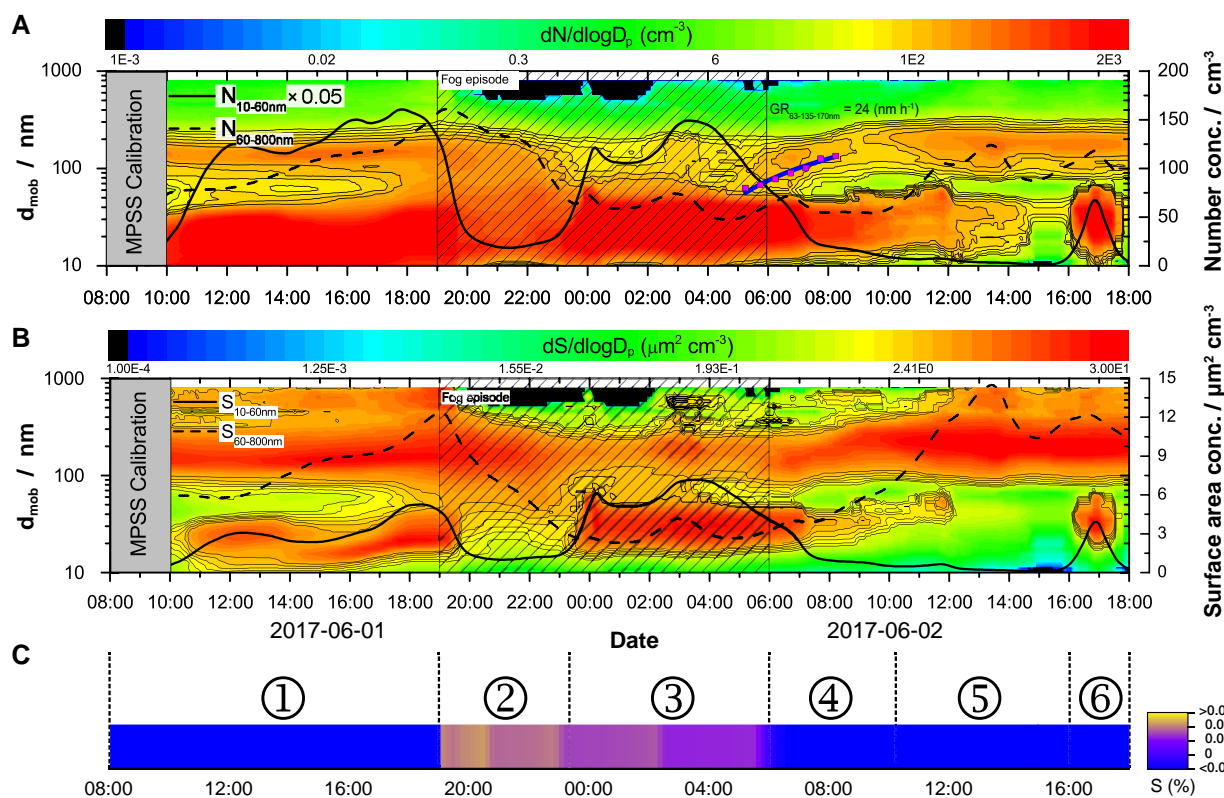


Fig. 1. A) Particle number and B) surface area size distribution, as well as integrated particle number and surface area concentrations. The PNC, integrated in different size ranges, can be found in Fig. S10. Fog episode duration (visibility $< 1,000$ m) is marked by the shaded area, while observed postfog particle growth is shown as an evolution of particle geometric mean diameter (fit based on squares from Fig. S3). C) Categorization of the measurement period (08:00, June 6 to 18:00, June 7) into six different characteristic periods and modeled S in model case 3.

In this study, the episode of 2017 June 1–2 was chosen for a case study because of the available comprehensive aerosol measurement data set, which involves both the microphysical and chemical properties of aerosol particles and fog droplets. Data for the episode between June 19 and 20 were limited, and therefore this episode was excluded from the further discussion in this study. For a more structured discussion of the June 1–2 episode, the event was divided into six distinct periods (in the text referred to as #1, #2, #3, etc.) reflecting the different conditions and co-occurring processes as shown in Fig. 1. The observed growth event of Aitken-mode particles started with NPF during period #1, recorded on June 1 at 6:00 UTC, when RV Polarstern was 80.4°N and 7.2°E (Fig. S1). Prior to the NPF events, the PNC decreased to 2 particles cm^{-3} and was associated with air masses prevailing from the North. The background particle number size distribution (PNSD) before the NPF event of June 1 was composed of two modes (Fig. S3). Because of NPF, the observed total PNC increased by two orders of magnitude: from background concentrations of 20 cm^{-3} on May 31 to $4,000 \text{ cm}^{-3}$ on June 1 (Fig. 1). Over 11 h (period #1), newly formed particles grew in size to the geometric mean diameter of 24 nm, forming a PNSD with three modes (see Fig. S3). Particle hygroscopicity several hours after the beginning of the NPF event (June 1, approximately 12:00 to 17:00 UTC) was $\kappa_{20\text{nm}} = 0.41 \pm 0.02$ and $\kappa_{150\text{nm}} = 0.52 \pm 0.1$. At 19:00 UTC, the fog episode began causing a perturbation in the PNSD. During the first part of the fog episode (period #2 in Fig. 1), the small particle (10–60 nm) surface area concentration [particle surface area size distribution (PSSD), see Fig. 1B] rapidly decreased (solid black line in Fig. 1A). This indicates that particles < 60 nm can initially be activated for about 3 to 4 h [activation of Aitken-mode particles requires high

S during the fog formation, which is possible under clean Arctic conditions (44)] and/or lost due to scavenging by fog droplets. Coagulation is unlikely to play an important role here due to relatively small Aitken and accumulation mode PNCs. Interestingly, about 3 to 4 h after the fog formation, the number concentration of < 60 nm particles recovered to a slightly lower level compared with prefog conditions indicating deactivation of smaller fog droplets or possible advection of nonfog processed particles. The increased surface area concentration suggests mass production by in-fog processes, which also increase particle size. During the second half of the fog episode (period #3 in Fig. 1), particles > 60 nm were still activated, as indicated by the small number of particles in this size range (Fig. 1A). After 4:00 UTC on June 2, as the measured visibility increased, the number concentration of particles < 60 nm began gradually decreasing for the next 4 h. In comparison, among particles with diameters > 60 nm, the number of particles increased. Later, the fog continued to dissipate and the measured visibility continued to increase until about 6:00 UTC (Fig. S4). PNSD showed a distinct growth of Aitken-mode particles to accumulation mode sizes (growing from ~ 60 to 170 nm in diameter) with a $\text{GR} > 20 \text{ nm h}^{-1}$ during the postfog period #4, illustrated by purple squares in Fig. 1A. This observed GR is much higher than reported values in the literature, e.g. 0.01 – 1.49 nm h^{-1} by Park et al. (26).

By 8:00 UTC, the number concentration of < 60 nm particles decreased to about 1/6 of the initial particle number at 4:00 UTC. Subsequently, the remaining PNSD comprised two modes (Fig. S3), resembling the shape of the observed background PNSD before the NPF event. Overall, because of the fog-related processes, the accumulation mode PNC increased by 14% (from

70 to 80 cm^{-3}). The hygroscopicity of newly formed accumulation mode particles was slightly lower— $\kappa_{150\text{nm}} = 0.43 \pm 0.06$, compared with hygroscopicity before the fog event. This suggests that organic compounds may be involved in particle growth to sizes above 60 nm, demonstrating that specific processes related to fog droplet chemistry could drive the growth of Aitken-mode particles. After the observed fog-induced rapid growth of Aitken-mode particles, the CCN concentration (associated with the background aerosol) increased by about 45%. Such an increase could affect the radiative properties of low-level clouds. A first-guess calculation has been performed to investigate this influence (see [supplementary material](#)). After 10:00 UTC (period #5), the PSSD showed dominant accumulation mode particles that can be CCN-active at relatively low S, allowing optically brighter clouds at low altitudes. The sudden appearance of a high concentration of smaller particles in period #6 was caused by RV emissions.

Fog-related multiphase chemistry modeling

To analyze the observed postfog growth of particles (<60 nm) and to find out what caused their growth into a size range where CCN activation is enabled without high S, three multiphase chemistry model simulations were carried out without (model case 1) and with (model cases 2 and 3) fog occurrences. The simulations focus solely on the long fog event between 2017 June 1 and 2, because of limited data availability for other events with longer fog duration after NPF. Two model cases with fog were simulated to distinguish between fogs with low (0.2%) and high (0.5%) S conditions during their formation.

In the fog formation phase, particles with a diameter of ≥ 102 nm are activated in model case 2 and particles with a diameter of ≥ 79 nm in model case 3. These activated particles are further named CCN-active particles. In model case 3, particles with diameters between >27 and <79 nm are partly activated for only a few hours; i.e. they are temporarily activated and deactivate after a while. These particles are named partly CCN-active particles and are only present in model case 3. Particles not activated in the model simulations are named CCN-inactive. Thus, in model case 2, CCN-inactive particles cover the size range of the Aitken-mode, whereas in model case 3, partly CCN-active particles dominate the Aitken-mode. An overview of the covered size ranges for the different simulations is provided in Table 1. All model investigations focused on the chemical processing during fog and the subsequent postfog periods.

Table 1. Specification of the different simulation cases.

Run identifier	Specification	Comment
Model case 1	No fog formation	
Model case 2	Fog formation with 0.2% supersaturation	CCN-inactive particles with diameter < 102 nm CCN-active particles with diameter ≥ 102 nm
Model case 3	Fog formation with 0.5% supersaturation	CCN-inactive particles with diameter ≤ 27 nm partly CCN-active particles with diameter between >27 and <79 nm CCN-active particles with diameter ≥ 79 nm

For the model cases with fog, a small increase in particle mass of about 75 and 71 ng m^{-3} was modeled at the end of the simulation for model cases 2 and 3, respectively (see Fig. S5). Due to clean conditions in the Arctic environment, characterized by low trace gas concentrations, fog chemistry-related mass increase is dominated by in-fog SO_2 oxidation. The simulations also indicate in-fog production of methanesulfonic acid (MSA), nitric acid, and oxalic acid (Fig. S6). Consistent with the results of Topping et al. (45) and their reported cocondensation process for pristine regions, an increase in dry mass is modeled during the early fog formation. During fog, the mass of Aitken-mode particles is simulated to decrease in model case 2 (CCN-inactive particles), while it is simulated to increase in model case 3 (partly CCN-active and CCN-active particles; see Fig. S5). However, an overall mass increase for Aitken-mode particles, such as in model case 3, is inconsistent with the in situ particle measurements (Fig. 1).

The mass decrease of CCN-inactive particles in model case 2 is related to the evaporation of SVCs from these particles to the undersaturated gas phase. This undersaturation results from the strong uptake of the soluble SVCs into the fog droplets, representing a stronger sink for SVCs compared with the gas-phase oxidation or the uptake to interstitial particles. The mass increase of Aitken-mode particles in model case 3 is then due to chemical in-fog production in partly activated particles (>27 to <79 nm in diameter). These dominate the fog droplet number for a short time period. As larger fog droplets grow at the expense of smaller ones, partly CCN-activated particles get deactivated after about 1.7 to 3.7 h increasing the number of Aitken-mode particles with a diameter <79 nm. This agrees also with the modeled decrease of S (Fig. 1). The modeled deactivation of smaller fog droplets is consistent with the observed particle number increase between 10 and 60 nm during June 1 (end of period #2 in Fig. 1). However, the fog and associated processes continued for another 4 h where advection of other aerosol/fog particles was possible. This implies that the particles during period #3 (Fig. 1) were not necessarily associated with the initial fog processing and high S as the particle size does not show an expected increase. Therefore, the simulation with lower S is more likely to represent these particles, and further discussion focuses on model case 2, as it appears to be more realistic for a long fog period (≥ 4 h).

The fog-related change in the dry mass concentration of CCN-inactive particles [$c(t)/c(t=5:40 \text{ UTC}, 2017-06-02)$] is displayed as a red line in Fig. S5. With fog dissipation, the model simulates a logarithmic increase of dry particle mass for the CCN-inactive particles (Fig. S5), which is in line with the in situ observations (period #4 in Fig. 1). The logarithmic increase is more strongly pronounced for model case 2 where particles ≤ 102 nm are not partly activated. At the end of the simulations, the dry mass is increased by a factor of about 1.1. In contrast, the positive slope is more linear in the simulation without fog occurrence, suggesting that fog chemistry plays a decisive role in the observed postfog-related growth processes of Aitken-mode particles.

To further investigate the processes responsible for the rapid increase of modeled CCN-inactive particle mass concentration (and thus their size), the predicted contribution of single chemical compounds to the observed growth was explored. In a pristine marine Arctic environment, the oxidation of DMS into MSA and sulfuric acid (H_2SO_4), as well as ammonia (NH_3) emission from the ocean surface, should be the most important drivers for particle growth. Ship-based emissions from RV Polarstern, rich in nitrogen oxides (NO_x), may also have contributed to particle growth through the fog-related aqueous phase HNO_3 formation. The modeled concentrations of MSA, ammonium, nitrate, and sulfate

in CCN-inactive and CCN-active particles, as well as particle mass increase related to fog evaporation, are shown in Figs. 2 and S7 for model cases 2 and 3, respectively. The orange color represents the sum of the modeled mass of CCN-active particles, and the violet is the sum of the modeled mass in CCN-inactive particles. The normalized mass increase due to fog is calculated for 5:40 UTC, because MSA evaporation from CCN-active particles and condensation onto CCN-inactive particles peaks at this time (see orange and violet area in Fig. 3 that represent the phase transfer flux of CCN-active and CCN-inactive particles, respectively). For CCN-inactive particles in model case 2, a rapid logarithmic increase of ammonium mass is simulated within the first 3 h after fog dissipation (from 6 to 9 AM, red line in Fig. 2A). This increase of about 0.6 ng m^{-3} corresponds to an increase of the ammonium mass by around one order of magnitude. The recondensation of ammonia, released from the evaporating fog droplets onto CCN-inactive particles, is fostered because of the higher acidity of the CCN-inactive particles compared with the CCN-active particles shortly after fog dissipation. Additionally, the simulation results reveal a strong logarithmic increase of MSA mass peaking around 12 AM following the ammonium mass increase for the CCN-inactive particles (purple area and red line in Fig. 2B), i.e. Aitken-mode particles in model case 2 and particles $\leq 27 \text{ nm}$ in model case 3. A logarithmic increase is also modeled for other dissolved semivolatile acids such as nitric acid and its dissociated form nitrate ($\text{HNO}_{3(\text{aq})} + \text{NO}_3^-$). As the density of MSA ($1,480 \text{ kg m}^{-3}$) is 80% of H_2SO_4 ($1,830 \text{ kg m}^{-3}$), the mass increase of MSA might also lower the overall density of the CCN-inactive particles and enhance an increase of the particle volume. At the end of the simulation, the mass of MSA is increased by a factor of 11 and 79 (with a peak value of 18 and 90) for model cases 2 and 3, respectively. This MSA mass increase is very interesting, as in general before fog occurrence, the model simulates MSA partitioning (average flux $2.8 \times 10^{-17} \text{ mol m}^{-3} \text{ s}^{-1}$) from the CCN-inactive (Aitken-mode) particles into the gas phase (Fig. 3). In contrast to this, all MSA from the gas phase is taken up into the fog droplets within the fog period thus triggering a phase transfer flux of MSA from the CCN-inactive particles to the gas phase (average flux $1.2 \times 10^{-16} \text{ mol m}^{-3} \text{ s}^{-1}$) and from the gas phase to fog droplets (average flux $2.5 \times 10^{-16} \text{ mol m}^{-3} \text{ s}^{-1}$) (repartitioning; Fig. 3). When the liquid fog water evaporates, the MSA concentration becomes oversaturated in the larger CCN-active particles and begins to evaporate around 5:40 AM into the gas phase. With fog dissipation, the MSA gas-phase concentration is $>6.0 \times 10^6$ molecules cm^{-3} , six times higher compared with the time period before the fog episode (red line in Fig. S6). The enhancement occurs because of an effective MSA production by aqueous-phase chemistry during the fog (28). Additionally, the modeled increase of gas-phase MSA is affected by higher acidity and lower liquid water content (LWC) of the CCN-active particles compared with fog droplets. From the gas phase, the MSA is then taken up by the particles before 11 AM with a maximum mass flux of $2.0 \times 10^{-15} \text{ mol m}^{-3} \text{ s}^{-1}$ at 5:50 AM leading to the modeled logarithmic increase in particulate MSA in the CCN-inactive particles. Around 8 AM, the mass flux toward the CCN-inactive particles decreases, whereas it begins to increase for CCN-active particles. Around 11 AM, the flux pattern changes, showing that the MSA evaporates from the CCN-inactive particles. The MSA transfer from the evaporating CCN-active particles to the CCN-inactive particles is also evident from Fig. S8, where the MSA mass in the different simulated aerosol size bins at 5:40 and 8 AM is shown. A logarithmic increase is not seen for sulfate (red line in Fig. 2C), a stronger and less-volatile acid than MSA (46), suggesting that sulfate

remains in the CCN-active and partly CCN-active particles and is not responsible for the observed growth. A logarithmic increase of the nitrate mass concentration in the CCN-inactive particles is also simulated. However, with the value of 0.1 ng m^{-3} , the modeled nitrate concentration in CCN-inactive particles is one order of magnitude lower than that of MSA (violet area in Fig. 2D). This indicates that nitrate is not likely to be a key driver of the observed particle growth. Nevertheless, Arctic climate change can induce higher ship traffic emissions and thus increases the importance and probability of nitrate-driven growth events.

The ability of the model to reproduce the distribution of key acids and bases between the different particle sizes was investigated by comparing the modeled data with Berner impactor measurement performed between 2017 June 1 and 4. As these values were also used to initialize the model, some technical issues were investigated to determine whether the approach was feasible. The relative concentrations of the measured compounds were used to initialize aerosol particle composition. Thus, the initial mass is not the same as the measured one. For example, the measured MSA mass in the impactor stage 1 (IS1) was 1.14 ng m^{-3} , while the initialized value was only 0.34 ng m^{-3} . This difference is caused by the initialized size distribution that is not representative for the whole measurement period of the impactor. Additionally, the flux investigation of MSA reveals that before the fog occurrence, the MSA in CCN-inactive particles from a size range of IS1 evaporates into the gas phase. The fog of interest occurred during the first part of the sampling period of the impactor. In the model, every particle size from the second IS is activated and grown to droplet diameters $> 10 \mu\text{m}$. Therefore, comparisons between modeled and measured concentrations for different IS of typical CCN sizes above 80 nm are limited. Activated and subsequently grown CCN particles were either not sampled due to their growth to larger sizes (above the cutoff size of the sampling inlet) or were sampled at a higher IS due to effective coagulation processes in the inlet system at very high RH. As the model does not consider the mentioned processes, only the comparison between model results and the first IS is discussed further.

Comparisons between measured concentrations of the Berner impactor and modeled values for model cases 2 and 3 are shown in Table S3. Special emphasis is put on MSA and nitrate as these are formed predominantly in the fog and can then recondense onto smaller particles. For the first IS, which includes the particle sizes affected by the observed volume increase, the modeled MSA is about a factor of 3 lower than the measurements for model case 2 (see Table S3). For nitrate, the detection limit is $<0.66 \text{ ng m}^{-3}$, and a concentration of 0.13 ng m^{-3} is modeled. An overestimation of more than one order of magnitude is modeled for MSA and nitrate in model case 3. This underlines the proposed conclusion that for longer fog episodes, model case 2 is more realistic. However, concentrations of sulfate and ammonium in the first and second IS are overestimated by the model by more than an order of magnitude for both model cases 2 and 3. This overestimation is explainable as the Berner impactor measurements, used to initialize the model, already contained the contribution from in-fog processes. Besides the Berner impactor measurements, the composition of fog droplets was also measured and compared with the modeled values. The comparison revealed that the model calculates less formate and oxalate as measured within the fog droplets, which might be related to missing emission sources or excessively low emissions within the model. A broader discussion of the comparisons is provided in the [supplementary material](#).

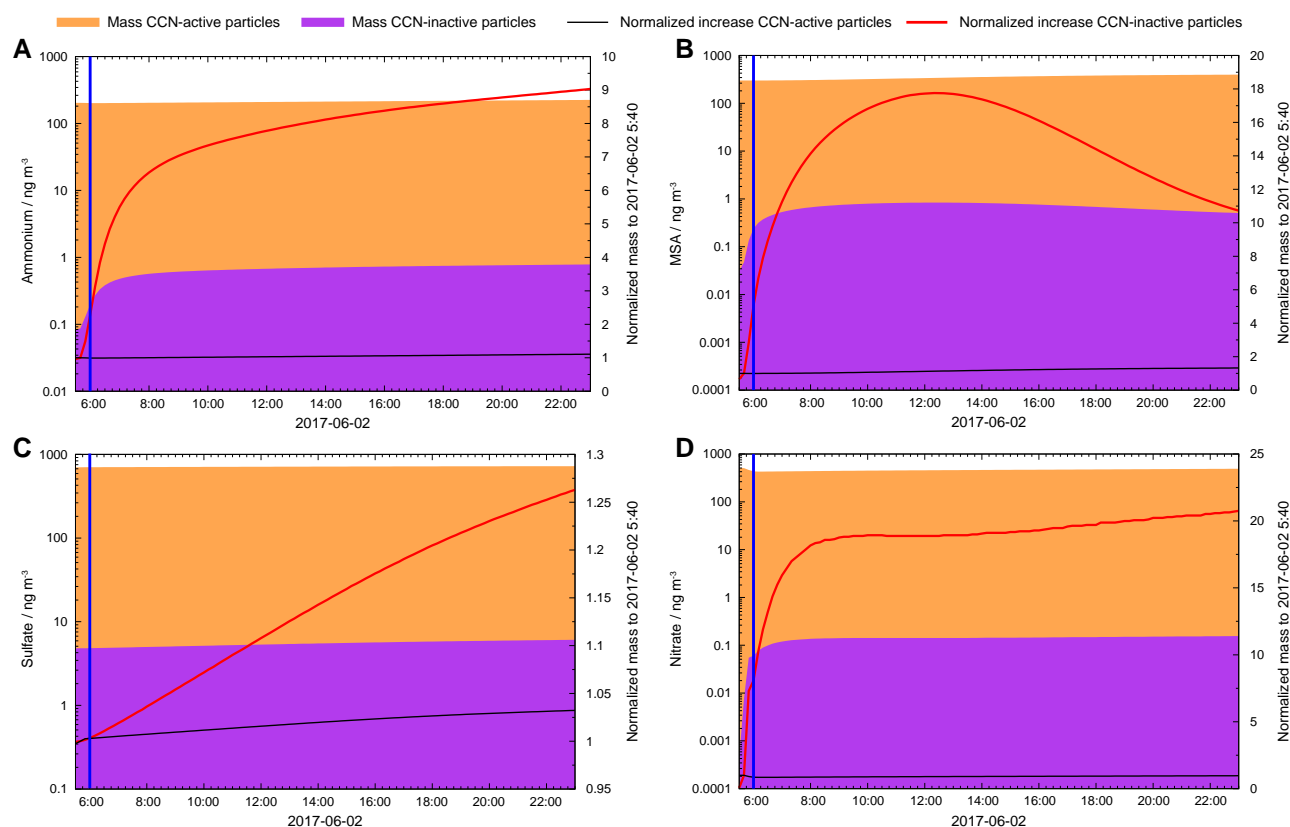


Fig. 2. Simulated concentration of particulate A) ammonium, B) methanesulfonate, C) sulfate, and D) nitrate after the fog period at June 2, 5:40 UTC ($t_{\text{model}} = 54.17$ h) for CCN-active and CCN-inactive particles for the model case 2. The normalized increase for the CCN-active and CCN-inactive particles is calculated as $c(t)/c(t = 5:40 \text{ UTC}, 2017-06-02)$. The blue line represents dissipation of the fog.

The measured concentration of MSA, given in Table S3, shows that MSA accounts for only about 1% to the measured IS1 mass. However, EC contributed about 25% to the measured mass during the long measurement period from June 1 to 4. The high EC content is caused by the ship exhaust emitted after the fog period. Since other compounds that condense onto particles may have been emitted in the process, it can be assumed that up to half of the measured mass might be due to ship exhaust. Thus, in the absence of this contamination, the MSA mass could contribute up to 2% of the total IS1 mass during the episode of interest. From the determined maximum normalized mass increase by a factor of 18 to 90 of MSA, a mass and volume increase of particles can be calculated. Considering a factor of 18, a particle volume increase factor of up to 1.36 can be calculated. Furthermore, assuming a constant density and spherical aerosol shape, an aerosol size increase can be determined. Thus, particles with a diameter of 60 nm can grow in size to 66 nm only by condensation of MSA.

However, this increase is still too small to explain the growth of the observed particles and should therefore be attributed to other SVCs. The comparison between the model IS1 data after the fog evaporation and the observational data reveals that the model underestimates the organic mass by about half. Unfortunately, detailed chemical information is unavailable to identify the main individual organic compounds contributing to the organic mass. On the other hand, the model has limitations in predicting in-fog formation of other oxidized organic compounds and/or their partitioning to the IS1 particles after the fog dissipation. Thus, the model underestimates the organic mass and the growth in diameter. Consequently, future measurements should focus on a more detailed determination of the organic mass composition,

the partitioning of semivolatile organic compounds, and the gas-phase concentration of potential precursors emitted by the ocean leading to organic mass.

In conclusion, the model results indicate that the observed particle growth is related to in-fog production of SVCs more volatile than sulfate. After fog evaporation, SVCs can partition from the larger fog-processed particles to the gas phase and then to recondense onto CCN-inactive particles initiating a rapid postfog growth process (Fig. 4). This process can predominantly occur after a longer fog duration when enough SVCs are formed, and the effect of high S is small. For short fog durations (<4 h) and fogs formed through higher turbulence, higher S can also activate particles with diameters > 27 nm, which might inhibit their rapid postfog growth, because these particles were already affected by fog chemistry and saturated with the formed SVCs.

Conclusion and implications

During an intensive field campaign in the summer Arctic, fog-related rapid growth ($\text{GR} > 20 \text{ nm h}^{-1}$) of newly formed particles to CCN relevant sizes (>80 nm) was observed. The process responsible for such particle growth can be important in explaining CCN number concentration in the Arctic and its impacts on the radiative forcing of Arctic low-level clouds. The underlying growth mechanism of 60 nm particles was investigated by combining in situ field measurements and multiphase chemistry modeling. The model investigations revealed that effective aqueous-phase chemistry in Arctic fog droplets can lead either directly to a mass increase of activated and grown particles or indirectly to a mass increase of nonactivated particles through the production

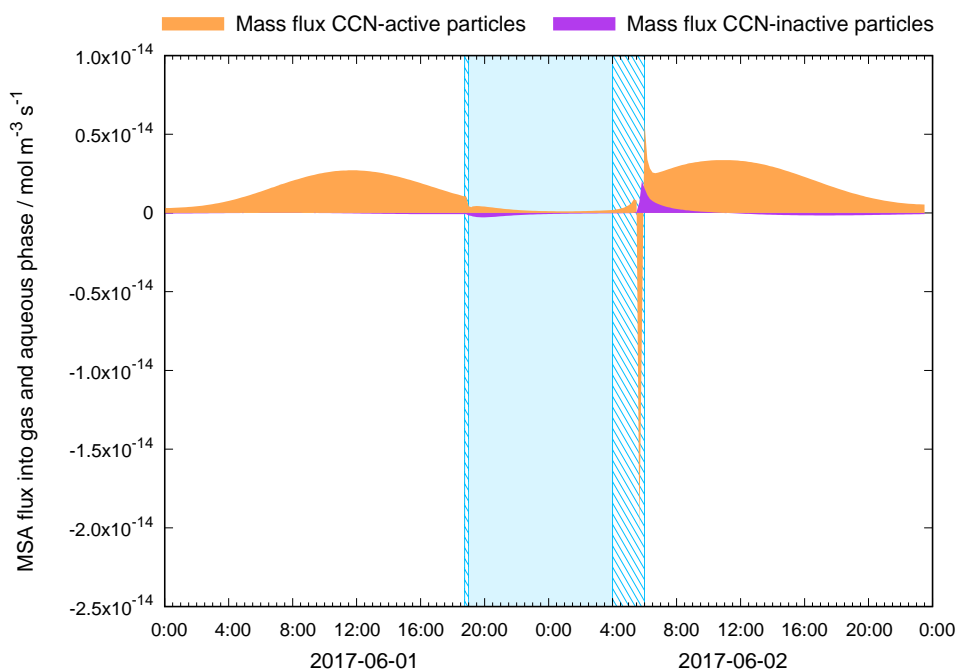


Fig. 3. Modeled mass flux of particulate MSA for the second and third model day within all size bins of CCN-active and CCN-inactive, respectively, for the model case 2. Here, MSA flux into gas phase is represented by negative, and MSA flux into aqueous phase is represented by positive values. The light blue and shaded blue bars represent fog and the formation and dissipation of the fog, respectively.

and postfog repartitioning of semivolatile acids (in particular MSA, but also nitrate and oxalic acid). These acids are formed within fog droplets by effective aqueous-phase chemistry. They can evaporate to some extent from the processed CCN-active particles during fog dissipation. With fog dissipation, the concentration in the gas phase was modeled to be enhanced by a factor of 6, 1.6, and 2 for MSA, nitric acid, and oxalic acid compared with the time before the fog formation, respectively. These semivolatile acids can immediately recondense onto the undersaturated CCN-inactive particles (Aitken-mode) along with semivolatile bases, mainly NH_3 . The observed rapid growth of 60 nm particles to sizes above 100 nm can be explained through this sequence of chemical in-fog production and physical repartitioning processes. In this context, the model simulations indicate S to be a key factor determining the observed rapid growth process during Arctic summer. For high modeled S (0.5%) which is more likely for clouds aloft of the ocean surface (33), very small Aitken-mode particles (diameter ~ 30 nm) can be activated and grow to droplet sizes, which allows in-cloud processing but inhibits subsequent rapid postfog growths. However, when lower S (0.2%) is modeled, which seems to represent a reasonable S estimate for Arctic fogs (33, 47), Aitken-mode particles are not activated and the repartitioning process is responsible for their rapid growth. Here, fog duration is a key variable. Longer fog duration enables chemical in-fog processes to produce more SVCs required for a postfog repartitioning. This in turn enables a stronger postfog growth of nonactivated Aitken-mode particles. The proposed fog-initiated growth mechanism is illustrated in Fig. 4. Due to a changing climate in the Arctic, the frequency and duration of fogs are increasing (39, 48, 49). As a result, the observed growth phenomena and proposed mechanism may have substantial implications to better understand the radiative forcing of Arctic low-level clouds.

The extent, frequency, and potential significance of this CCN formation process need to be further investigated through the additional combined field, laboratory, and modeling studies.

Future field studies in the summer Arctic should focus on highly time-resolved measurements of aerosol and cloud microphysics in parallel with advanced chemical analysis techniques to characterize important gas-phase components, as well as aerosol and fog droplet compositions. Particular emphasis should be dedicated to time-resolved measurements of semivolatile acids and bases in all phases. Consequently, further evidence for the proposed growth mechanism and its relevance can be provided. In perspective, advanced parameterizations need to be developed to incorporate fog-driven CCN formations in global climate models to improve model predictions on Arctic amplification.

Materials and methods

Field measurements

The field measurement results presented here were collected onboard the RV *Polarstern* during the first leg of the expedition named “Physical feedbacks of Arctic boundary layer, Sea ice, Cloud and Aerosol (PASCAL, PS 106/1)” (18). The cruise track and geographical location of the discussed event, alongside with other relevant information are presented in Fig. S9.

Continuous measurements of PNSDs in a size range from 3 to 800 nm were made using a neutral cluster and air ion spectrometer (NAIS, 2 to 10 nm) (50) and a TROPOS-type mobility particle size spectrometer (MPSS, 10 to 800 nm) (51). Size-segregated (15 to 150 nm) particle hygroscopicity at subsaturation (90% RH) was measured using a TROPOS-type volatility-hygroscopicity tandem differential mobility analyzer (VHTDMA). Aerosol sample RH < 40% was ensured with a membrane dryer.

For offline chemical analysis, aerosol particles were sampled at the side wall of the measurement container using five-stage (0.05–0.14, 0.14–0.42, 0.42–1.2, 1.2–3.5, and 3.5–10 μm of aerodynamic particle diameter) low-pressure Berner impactors (Hauke, Austria). Sampling lines were heated to $\Delta T_{\text{max}} = 9^\circ\text{C}$ to

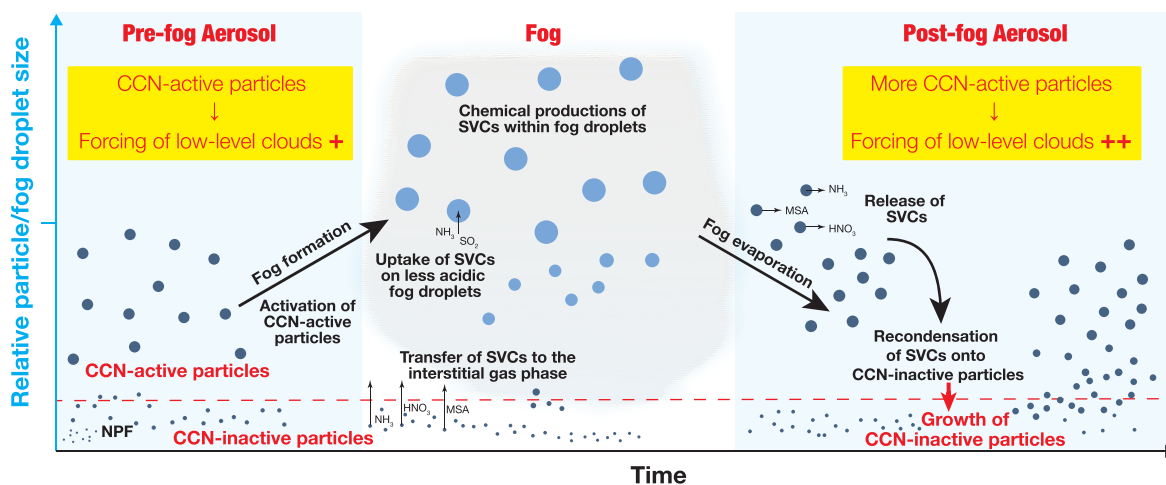


Fig. 4. Illustration of processes involved in the postfog growth of Aitken-mode (CCN-inactive) particles due to the recondensation of SVCs. The implications for the radiative forcing, i.e. the supposed changes in cloud albedo and related radiation effects are also shown.

reduce sample humidity to 75–80% RH, while minimizing the losses of the species discussed. An isokinetic inlet at a flow rate of 75 L min^{-1} was used. Size-segregated aerosol particles were collected on preheated (350°C for at least 2 h) aluminum foils.

Fog samples were collected using the Caltech Active Strand Cloud Collector Version 2 (CASCC2). Cloud droplets were sampled on the strands and gravitationally channeled into a Nalgene bottle. The 50% lower size cut for the CASCC2 is $\sim 3.5\text{-}\mu\text{m}$ diameter (52). More details of the cloud-water sampling procedure can be found in Hartmann et al. (53). Supplementary meteorological parameters, such as global radiation, temperature, and RH were measured by the autonomous ship weather station.

Multiphase chemistry simulations

Simulations with the SPectral Aerosol Cloud Chemistry Interaction Model (SPACCIM) framework (54) were carried out to examine the impact of multiphase chemistry on the observed particle growth. Detailed gas- and aqueous-phase chemistry is resolved by the Master Chemical Mechanism (MCMv3.2, <http://mcm.york.ac.uk/>) coupled to the Chemical Aqueous Phase Radical Mechanism (CAPRAM4.0) (55). Halogen chemistry is described by CAPRAM-HM2.1 (56) and DMS chemistry by CAPRAM-DM1.0 (28). Additionally, uptake and dissociation of monomethylamine and trimethylamine (57, 58), the dominant emitted amines from the ocean into the atmosphere, have been included to better represent aerosol acidity evolution. For the simulations, an air parcel moves along a predefined trajectory for 72 h. Note that the simulations were performed using local time. Temperature is fixed at $T = -2^\circ\text{C}$ and $\text{RH} = 95\%$ to be consistent with the measured average values for the period of interest (2017 June 1–2). The first 24 h are used as model spin-up. Within the second model day, the fog occurrence is included. Fog formation is realized in the model by an adiabatic cooling of the air parcel for a certain time that occurs after 43.25 h (model case 2) and after 43.48 h (model case 3) of modeling time. Thereby, the amount of adiabatic cooling defines the modeled S leading to a S of 0.2 and 0.5% in model cases 2 and 3 during fog formation. At 43.5 h (corresponding to June 1, 19:00 UTC), fog is formed, which resides until 52.5 h (June 2, 4:00 UTC). For model case 2, particles $\geq 102 \text{ nm}$ and, for model case 3, particles $> 27 \text{ nm}$ in diameter were activated, respectively. In the model case 3, smaller particles (between >27 and $<79 \text{ nm}$ in diameter) are activated to fog droplets

that shrink shortly after activation back to particle sizes because the water condenses more efficiently onto the bigger droplets with ongoing simulation time, and the S is reduced so that such particles are deactivated. The slow fog dissipation is simulated by an adiabatic warming of the air parcel for 2 h until 54.5 h model time (June 2, 6:00 UTC). Time was converted to UTC (measurement time) for data presentation. To investigate the observed particle size growth, the model was initialized using the in situ measured PNSD during the fog dissipation (Fig. S3C). This distribution is fixed in the box model, and thus, the discussed results on size evolution are qualitative of nature. The chemical composition of aerosol particles included is determined from impactor measurements from June 1 to 4 (Table S2). During that time, a stable inflow from the west was observed, i.e. no air mass change during the sampling. The initialized aerosol composition contains the relative contributions to the aerosol mass derived from the measured individual compound masses and the total particulate mass. Gas-phase model initialization of volatile organic compounds and inorganic trace gases such as NO_x is based on the two measurement stations at Ny-Ålesund (code numbers NO1665R and NO0042G), as well as on a literature survey of background concentrations during Arctic summer (see Table S1). Anthropogenic emission values of 2017 June along the trajectory are taken from the Atmospheric Chemistry and Climate Model Inter-comparison Project (ACCMIP) (59) inventory. Natural emissions from the Arctic Ocean surface are initialized from literature studies (60), except DMS for which a monthly mean for 2017 June was used. The DMS emission was calculated online in a previous study (61). Emissions from snowpack and dry deposition values of gases were initialized following Piot and von Glasow (62) and Zhou et al. (63). The whole model initialization data are summarized in Table S1. To evaluate the model prediction accuracy, the simulated chemical compound concentrations were compared with measured ones (Tables S3 and S4).

Data evaluation, trajectory model, and satellite data

Electrical particle mobility measured by a NAIS instrument was inverted to particle mobility diameter using the v14-Irmd inversion algorithm (64). MPSS data were inverted by following the respective inversion algorithm (65). Particle transmission losses and counting efficiency were accounted for in preparing final particle

and ion number size distributions (51, 66, 67) To clear MPSS measurement data from ship pollution, the sliding 25th percentile filter over a window of 1 h and 30 min (corresponding to 18 measurement points) was applied. Particle GR were calculated utilizing methodology by Kulmala et al. (68). The DMAinv routine (69) was used to invert VHTDMA data. The computed hygroscopic growth factor was used to parameterize particle hygroscopicity by κ -Köhler theory (70).

For laboratory particle chemical analysis, ion chromatography (ICS3000, Dionex, Sunnyvale, CA, USA) was used (71). Sea salt sulfate (ss-sulfate) was calculated from the constant mass ratio $m(\text{SO}_4^{2-})/m(\text{Na}^+) = 0.25$ in bulk seawater (72). The data analysis was performed using the R programming language and free software environment for statistical computing and graphics (73). Backward air mass trajectories were calculated using HYSPLIT (74). The chlorophyll-*a* mass concentration in surface water (product OCEANCOLOUR_ARC_CHL_L3_REP_OBSERVATIONS_009_069) is taken from E.U. Copernicus Marine Service (<http://marine.copernicus.eu/>, last access: 2021 April 6). Cloud/fog coverage is taken from NASA Worldview (<https://worldview.earthdata.nasa.gov>, last access: 2021 April 6; VIIRS product).

Acknowledgments

The authors would like to thank Andreas Macke (TROPOS) and Hauke Flores (AWI), Chief Scientists of PS106 cruise, Thomas Wunderlich—the Captain, as well as the RV Polarstern crew for logistic support. The authors also thank Susanne Fuchs for the ion chromatography measurements. The authors acknowledge the EBAS/NILU database (<https://ebas-data.nilu.no/Default.aspx>) and the Norwegian Institute for Air Research (NILU) for providing measurement data from Ny-Alesund and Zeppelin Mountain site used for the initialization of the model. The authors gratefully acknowledge the NOAA Air Resources Laboratory (ARL) for the provision of the HYSPLIT transport and dispersion model and/or READY website (<https://www.ready.noaa.gov>) used in this publication.

Supplementary material

Supplementary material is available at PNAS Nexus online.

Funding

The authors would like to acknowledge the funding of the Deutsche Forschungsgemeinschaft (DFG, German Research Foundation)—project number 268020496—TRR 172, within the Transregional Collaborative Research Center “Arctic Amplification: Climate Relevant Atmospheric and Surface Processes, and Feedback Mechanisms (AC)³, and the funding of RV Polarstern cruise PS106 (expedition grant number AWI-PS-106-00) by Alfred Wegener Institute for Polar and Marine Research (AWI). E.H.H., M.v.P., and H.H. acknowledge funding by DFG under project ORIGAMY (project number: 447349939 (HE 3086/45-1)). S.Z. and M.v.P. gratefully acknowledge funding by DFG (project number 268020496—TRR 172) within AC³ (subproject B04). M.K. acknowledges the ACCC Flagship funded by the Academy of Finland (337549). The INAR project “Quantifying carbon sink, CarbonSink+ and their interaction with air quality” funded by Jane and Aatos Erkkö Foundation, and the European Research Council (ERC) project ATM-GTP Contract (742206) are as well acknowledged. C.B.-V. acknowledges the funding from Bundesministerium für Bildung und Forschung for the

project Combining MOSAiC and Satellite Observations for Radiative Closure and Climate Implications (MOSARiCs) (project number 03F0890A).

Author contributions

S.K., E.H.H., and A.T. designed the research; S.K., E.H.H., A.T., C.B.-V., L.M., M.L., M.v.P., S.Z., and T.V. performed the research; H.H., A.W., M.K., and P.P. contributed new materials and analytic tools; S.K., E.H.H., and A.T. analyzed the data, discussed the results and their adequate interpretation with H.H., and wrote the paper to which all authors then contributed. All authors discussed the results obtained.

Data availability

Field data are available on the public repository: <https://doi.pangaea.de/10.1594/PANGAEA.932569> (ion data for aerosol particles) and <https://doi.pangaea.de/10.1594/PANGAEA.932573> (ion data for fog water).

References

- 1 Jeffries MO, Overland JE, Perovich DK. 2013. The Arctic shifts to a new normal. *Phys Today*. 66(10):35–40.
- 2 Richter-Menge J, Overland JE, Mathis JT, Osborne E. 2017. Arctic report card 2017. NOAA. https://arctic.noaa.gov/Portals/7/ArcticReportCard/Documents/ArcticReportCard_full_report_2017.pdf.
- 3 Stroeve JC, et al. 2012. The Arctic's rapidly shrinking sea ice cover: a research synthesis. *Clim Change*. 110(3–4):1005–1027.
- 4 Bi HB, et al. 2018. Arctic sea ice volume changes in terms of age as revealed from satellite observations. *IEEE J Stars*. 11(7):2223–2237.
- 5 Polashenski C, et al. 2017. Percolation blockage: a process that enables melt pond formation on first year Arctic sea ice. *J Geophys Res Oceans*. 122(1):413–440.
- 6 Rampal P, Weiss J, Marsan D. 2009. Positive trend in the mean speed and deformation rate of Arctic sea ice, 1979–2007. *J Geophys Res Oceans*. 114(C5):C05013.
- 7 Meier WN, et al. 2014. Arctic Sea ice in transformation: a review of recent observed changes and impacts on biology and human activity. *Rev Geophys*. 52(3):185–217.
- 8 Cohen J, et al. 2014. Recent Arctic amplification and extreme mid-latitude weather. *Nat Geosci*. 7(9):627–637.
- 9 Serreze MC, Barry RG. 2011. Processes and impacts of Arctic amplification: a research synthesis. *Global Planet Change* 77(1–2): 85–96.
- 10 Whiteman G, Hope C, Wadhams P. 2013. Vast costs of Arctic change. *Nature* 499(7459):401–403.
- 11 Bekkers E, Francois JF, Rojas-Romagosa H. 2018. Melting ice caps and the economic impact of opening the northern sea route. *Econ J*. 128(610):1095–1127.
- 12 Hong N. 2012. The melting Arctic and its impact on China's maritime transport. *Res Transp Econ*. 35(1):50–57.
- 13 Bennartz R, et al. 2013. July 2012 Greenland melt extent enhanced by low-level liquid clouds. *Nature* 496(7443):83–86.
- 14 Shupe MD, Intrieri JM. 2004. Cloud radiative forcing of the Arctic surface: the influence of cloud properties, surface albedo, and solar zenith angle. *J Clim*. 17(3):616–628.
- 15 Loewe K. 2017. *Arctic mixed-phase clouds : macro- and microphysical insights with a numerical model*. Karlsruhe: KIT Scientific Publishing. p. 140.

- 16 Mioche G, et al. 2017. Vertical distribution of microphysical properties of Arctic springtime low-level mixed-phase clouds over the Greenland and Norwegian seas. *Atmos Chem Phys*. 17(20): 12845–12869.
- 17 Shupe MD, Matrosov SY, Uttal T. 2006. Arctic mixed-phase cloud properties derived from surface-based sensors at SHEBA. *J Atmos Sci*. 63(2):697–711.
- 18 Wendisch M, et al. 2019. The Arctic cloud puzzle: using ACLOUD/PASCAL multiplatform observations to unravel the role of clouds and aerosol particles in Arctic amplification. *B Am Meteorol Soc*. 100(5):841–872.
- 19 Mauritsen T, et al. 2011. An Arctic CCN-limited cloud-aerosol regime. *Atmos Chem Phys*. 11(1):165–173.
- 20 Kecorius S, et al. 2019. New particle formation and its effect on cloud condensation nuclei abundance in the summer Arctic: a case study in the Fram Strait and Barents Sea. *Atmos Chem Phys*. 19(22):14339–14364.
- 21 Nieminen T, et al. 2018. Global analysis of continental boundary layer new particle formation based on long-term measurements. *Atmos Chem Phys*. 18(19):14737–14756.
- 22 Baccarini A, et al. 2020. Frequent new particle formation over the high Arctic pack ice by enhanced iodine emissions. *Nat Commun*. 11(1):4924.
- 23 Kerminen V-M, et al. 2018. Atmospheric new particle formation and growth: review of field observations. *Environ Res Lett*. 13(10):103003.
- 24 Ghahremaninezhad R, et al. 2019. Dimethyl sulfide and its role in aerosol formation and growth in the Arctic summer—a modeling study. *Atmos Chem Phys*. 19(23):14455–14476.
- 25 Ghahreman R, et al. 2021. Modeling aerosol effects on liquid clouds in the summertime Arctic. *J Geophys Res Atmos*. 126(24): e2021JD034962.
- 26 Park KT, et al. 2021. Dimethyl sulfide-induced increase in cloud condensation nuclei in the Arctic atmosphere. *Glob Biogeochem Cycles*. 35(7):e2021GB006969.
- 27 Burkart J, et al. 2017. Organic condensation and particle growth to CCN sizes in the summertime marine Arctic is driven by materials more semivolatile than at continental sites. *Geophys Res Lett*. 44(20):10725–10734.
- 28 Hoffmann EH, et al. 2016. An advanced modeling study on the impacts and atmospheric implications of multiphase dimethyl sulfide chemistry. *Proc Natl Acad Sci U S A*. 113(42):11776–11781.
- 29 Revell LE, et al. 2019. The sensitivity of Southern Ocean aerosols and cloud microphysics to sea spray and sulfate aerosol production in the HadGEM3-GA7.1 chemistry–climate model. *Atmos Chem Phys*. 19(24):15447–15466.
- 30 Abbatt JPD, et al. 2019. Overview paper: new insights into aerosol and climate in the Arctic. *Atmos Chem Phys*. 19(4):2527–2560.
- 31 Komppula M, Lihavainen H, Kerminen V-M, Kulmala M, Viisanen Y. 2005. Measurements of cloud droplet activation of aerosol particles at a clean subarctic background site. *J Geophys Res Atmos*. 110(D6):D0620.
- 32 Croft B, et al. 2016. Contribution of Arctic seabird-colony ammonia to atmospheric particles and cloud-albedo radiative effect. *Nat Commun*. 7:13444.
- 33 Leitch WR, et al. 2016. Effects of 20–100 nm particles on liquid clouds in the clean summertime Arctic. *Atmos Chem Phys*. 16(17):11107–11124.
- 34 Pöhlker ML, et al. 2021. Aitken mode particles as CCN in aerosol- and updraft-sensitive regimes of cloud droplet formation. *Atmos Chem Phys*. 21(15):11723–11740.
- 35 Kerminen VM, et al. 2012. Cloud condensation nuclei production associated with atmospheric nucleation: a synthesis based on existing literature and new results. *Atmos Chem Phys*. 12(24): 12037–12059.
- 36 Koike M, et al. 2019. Year-round in situ measurements of Arctic low-level clouds: microphysical properties and their relationships with aerosols. *J Geophys Res Atmos*. 124(3):1798–1822.
- 37 Egerer U, Siebert H. 2019. Ultrasonic anemometer turbulence measurements at 10 m during a PASCAL ice station on POLARSTERN cruise PS106/1 PANGAEA, <https://doi.org/10.1594/PANGAEA.899232>.
- 38 Egerer U, Gottschalk M, Siebert H, Ehrlich A, Wendisch M. 2019. The new BELUGA setup for collocated turbulence and radiation measurements using a tethered balloon: first applications in the cloudy Arctic boundary layer. *Atmos Meas Tech*. 12(7): 4019–4038.
- 39 Danielson RE, Zhang M, Perrie WA. 2020. Possible impacts of climate change on fog in the Arctic and subpolar North Atlantic. *Adv Stat Climatol Meteorol Oceanogr*. 6(1):31–43.
- 40 Dall'Osto M, et al. 2017. Arctic Sea ice melt leads to atmospheric new particle formation. *Sci Rep*. 7(1):3318.
- 41 Dall'Osto M, et al. 2018. Regions of open water and melting sea ice drive new particle formation in North East Greenland. *Sci Rep*. 8(1):6109.
- 42 Mioche G, Jourdan O, Ceccaldi M, Delanoe J. 2015. Variability of mixed-phase clouds in the Arctic with a focus on the Svalbard region: a study based on spaceborne active remote sensing. *Atmos Chem Phys*. 15(5):2445–2461.
- 43 Wu DL, Lee JN. 2012. Arctic low cloud changes as observed by MISR and CALIOP: implication for the enhanced autumnal warming and sea ice loss. *J Geophys Res Atmos*. 117(D7):D0710.
- 44 Willis MD, et al. 2016. Growth of nucleation mode particles in the summertime Arctic: a case study. *Atmos Chem Phys*. 16(12): 7663–7679.
- 45 Topping D, Connolly P, McFiggans G. 2013. Cloud droplet number enhanced by co-condensation of organic vapours. *Nat Geosci*. 6(6):443–446.
- 46 Kreidenweis SM, Seinfeld JH. 1988. Nucleation of sulfuric-acid water and methanesulfonic-acid water solution particles—implications for the atmospheric chemistry of organosulfur species. *Atmos Environ*. 22(2):283–296.
- 47 Martin M, et al. 2011. Cloud condensation nuclei closure study on summer Arctic aerosol. *Atmos Chem Phys*. 11(22):11335–11350.
- 48 Klein SA, Hartmann DL. 1993. The seasonal cycle of low strati-form clouds. *J Clim*. 6(8):1587–1606.
- 49 Nilsson DE, Bigg KE. 2017. Influences on formation and dissipation of high Arctic fogs during summer and autumn and their interaction with aerosol. *Tellus B Chem Phys Meteorol*. 48(2): 234–253.
- 50 Mirme S, Mirme A. 2013. The mathematical principles and design of the NAIS—a spectrometer for the measurement of cluster ion and nanometer aerosol size distributions. *Atmos Meas Tech*. 6(4): 1061–1071.
- 51 Wiedensohler A, et al. 2012. Mobility particle size spectrometers: harmonization of technical standards and data structure to facilitate high quality long-term observations of atmospheric particle number size distributions. *Atmos Meas Tech*. 5(3):657–685.
- 52 Demoz BB, Collett JL, Daube BC. 1996. On the caltech active strand cloudwater collectors. *Atmos Res*. 41(1):47–62.
- 53 Hartmann M, et al. 2021. Terrestrial or marine—indications towards the origin of ice-nucleating particles during melt season in the European Arctic up to 83.7° N. *Atmos Chem Phys*. 21(15): 11613–11636.

- 54 Wolke R, et al. 2005. SPACCIM: a parcel model with detailed microphysics and complex multiphase chemistry. *Atmos Environ.* 39(23–24):4375–4388.
- 55 Bräuer P, et al. 2019. Development of a protocol for the auto-generation of explicit aqueous-phase oxidation schemes of organic compounds. *Atmos Chem Phys.* 19(14):9209–9239.
- 56 Hoffmann EH, Tilgner A, Wolke R, Herrmann H. 2019. Enhanced chlorine and bromine atom activation by hydrolysis of halogen nitrates from marine aerosols at polluted coastal areas. *Environ Sci Technol.* 53(2):771–778.
- 57 Ge XL, Wexler AS, Clegg SL. 2011. Atmospheric amines—part II. Thermodynamic properties and gas/particle partitioning. *Atmos Environ.* 45(3):561–577.
- 58 Sander R. 2015. Compilation of Henry's Law constants (version 4.0) for water as solvent. *Atmos Chem Phys.* 15(8):4399–4981.
- 59 Lamarque JF, et al. 2010. Historical (1850–2000) gridded anthropogenic and biomass burning emissions of reactive gases and aerosols: methodology and application. *Atmos Chem Phys.* 10(15):7017–7039.
- 60 Bräuer P, Tilgner A, Wolke R, Herrmann H. 2013. Mechanism development and modelling of tropospheric multiphase halogen chemistry: the CAPRAM Halogen Module 2.0 (HM2). *J Atmos Chem.* 70(1):19–52.
- 61 Hoffmann EH, Heinold B, Kubin A, Tegen I, Herrmann H. 2021. The importance of the representation of DMS oxidation in global chemistry-climate simulations. *Geophys Res Lett.* 48(13):e2021GL094068.
- 62 Piot M, von Glasow R. 2008. The potential importance of frost flowers, recycling on snow, and open leads for ozone depletion events. *Atmos Chem Phys.* 8(9):2437–2467.
- 63 Zhou XL, et al. 2001. Snowpack photochemical production of HONO: a major source of OH in the Arctic boundary layer in springtime. *Geophys Res Lett.* 28(21):4087–4090.
- 64 Wagner R, et al. 2016. On the accuracy of ion measurements using a neutral cluster and air ion spectrometer. *Boreal Environ Res.* 21(3–4):230–241.
- 65 Pfeifer S, et al. 2014. A fast and easy-to-implement inversion algorithm for mobility particle size spectrometers considering particle number size distribution information outside of the detection range. *Atmos Meas Tech.* 7(1):95–105.
- 66 Wiedensohler A, et al. 2017. Mobility particle size spectrometers: calibration procedures and measurement uncertainties. *Aerosol Sci Tech.* 52(2):146–164.
- 67 Wiedensohler A, et al. 1997. Intercomparison study of the size-dependent counting efficiency of 26 condensation particle counters. *Aerosol Sci Tech.* 27(2):224–242.
- 68 Kulmala M, et al. 2012. Measurement of the nucleation of atmospheric aerosol particles. *Nat Protoc.* 7(9):1651–1667.
- 69 Gysel M, McFiggans GB, Coe H. 2009. Inversion of tandem differential mobility analyser (TDMA) measurements. *J Aerosol Sci.* 40(2):134–151.
- 70 Petters MD, Kreidenweis SM. 2007. A single parameter representation of hygroscopic growth and cloud condensation nucleus activity. *Atmos Chem Phys.* 7(8):1961–1971.
- 71 Müller K, et al. 2010. Particle characterization at the Cape Verde atmospheric observatory during the 2007 RHaMBLe intensive. *Atmos Chem Phys.* 10(6):2709–2721.
- 72 Fomba KW, et al. 2014. Long-term chemical characterization of tropical and marine aerosols at the Cape Verde Atmospheric Observatory (CVAO) from 2007 to 2011. *Atmos Chem Phys.* 14(17):8883–8904.
- 73 R-Core Team. 2015. R: a language and environment for statistical computing. Vienna, Austria: R Foundation for Statistical Computing. <https://www.R-project.org/>.
- 74 Cohen MD, et al. 2015. NOAA's HYSPLIT atmospheric transport and dispersion modeling system. *B Am Meteorol Soc.* 96(12):2059–2077.